January 5, 2015

A 24μm Point Source Catalog of the Galactic Plane from Spitzer/MIPSGAL

R. A Gutermuth, *University of Massachusetts - Amherst*
Mark Heyer

A 24μm Point Source Catalog of the Galactic Plane from Spitzer/MIPSGAL.

Robert A. Gutermuth
and
Mark Heyer

Department of Astronomy, University of Massachusetts, Amherst, MA 01003

ABSTRACT

In this contribution, we describe the applied methods to construct a 24μm-based point source catalog derived from the image data of the MIPSGAL 24μm Galactic Plane Survey and the corresponding data products. The high quality catalog product contains 933,818 sources, with a total of 1,353,228 in the full archive catalog. The source tables include positional and photometric information derived from the 24μm images, source quality and confusion flags and counterpart photometry from matched 2MASS, GLIMPSE, and WISE point sources. Completeness decay data cubes are constructed at 1′ angular resolution that describe the varying background levels over the MIPSGAL field and the ability to extract sources of a given magnitude from this background. The completeness decay cubes are included in the set of data products. We present the results of our efforts to verify the astrometric and photometric calibration of the catalog, and present several analyses of minor anomalies in these measurements to justify adopted mitigation strategies.

Subject headings: survey: Milky Way

1. Introduction

The MIPSGAL Survey is a Legacy Program of the Spitzer Space Telescope that imaged the 24 and 70μm emission along the inner disk of the Milky Way (Carey et al. 2009). These mid-infrared bands are sensitive to the thermal emission radiated by interstellar dust grains that reside within a broad range of environments such as the envelopes of evolved stars, circumstellar disks and infalling envelopes surrounding young stellar objects, HII regions, supernova remnants, and the extended domains of dense, interstellar clouds. As a wide area survey, MIPSGAL is an important component to the infrared-to-millimeter reconnaissance of the Galaxy, which includes recent, all-sky missions: 2MASS (Skrutskie et al. 2006), WISE (Wright et al. 2010), and Planck (Planck Collaboration et al. 2011) as well as surveys targeted along the Galactic plane: GLIMPSE (Churchwell et al. 2009), ATLASGAL (Schuller et al.

2009), the Bolocam Galactic Plane Survey (Aguirre et al. 2011; Ginsburg et al. 2013) and the Herschel Infrared Galactic Plane Survey (Molinari et al. 2010). With its primary 24μm band[1], MIPSGAL provides a critical wavelength measurement, which links the near infrared data from 2MASS and GLIMPSE to the far-infrared/submillimeter information for both point sources and diffuse emission.

The processed, 24μm MIPSGAL image mosaics have been available since 2008 (Carey et al. 2009). This data product is comprised of flux calibrated FITS images of 24μm surface brightness with astrometric header information, images of the surface brightness standard deviations of the coadded data, data coverage and locations of problematic

---

[1]Operational non-linearities in the MIPS 70μm system resulted in much reduced sensitivities. The Spitzer 70μm data are superseded by the Herschel/PACS system and are not included in the MIPSGAL catalog described in this contribution.

data. Each mosaic field (hereafter, a tile) covers $\sim 1 \times 1$ deg^2 area.

As much of the measured MIPSGAL 24μm signal resides within an unresolved component (evolved stars, young stellar objects, compact clusters), a previously missing yet critical data product is a point source catalog derived from the image tiles. The value of a source catalog lies within the uniformity of the source extraction and photometry algorithms applied to all image data and the evaluation of source completeness. The compilation of source positions, fluxes, flux errors, and completeness limits enables a more comprehensive, condensed examination of 24μm emitting objects in the Galaxy. When merged with photometry from other surveys, one can further select for certain types of objects based on the shape of the spectral energy distribution and flux amplitude.

In this contribution, we describe the construction of a 24μm-based source catalog derived from MIPSGAL data. In §2, the source extraction and aperture photometry methods are summarized. The photometric accuracies, calibration, and catalog completeness are evaluated in reference to the literature in §3. In §4, we describe the method to derive 24μm source completeness limit for each MIPSGAL tile. The columns of the source catalog table are defined in the Appendix.

2. Building the 24μm Point Source Catalog

Here we describe in detail the methods used in the construction of the inclusive "archive" and high reliability "catalog" photometry tables using the MIPSGAL 24μm image tiles. In summary, we find compact sources in all tiles, measure their 24μm photometric properties, merge the tile lists together, and link the results to external catalogs. Astrometric systematics are examined in order to correct calibration offsets by tile and establish conditions for a confusion flag that is internal to our source list.

2.1. Source Extraction

The MIPSGAL image tile products are extremely uniform integration depth maps of 24μm flux density, but robust point source detection is nontrivial because of nonuniform background emission across the Milky Way. For a large sur-

vey such as MIPSGAL, automated data analysis techniques are essential. However, many automated point source detection techniques produce substantial numbers of false detections among the filamentary emission structures of the nebulae surrounding recent star forming events. Here, we have adopted the IDL program PhotVis (version 1.10) to robustly identify point-like sources regardless of the complexity of the background (Gutermuth et al. 2008).

PhotVis employs a modified version of the DAOFIND source detection algorithm (Stetson 1987), as implemented in the IDL Astronomy Users' Library (Landsman 1993). In summary, the DAOFIND technique involves convolving each image with a "sunken" two dimensional Gaussian function sized to match the beam size of the observations (for this work, 6.25″ full-width at half-maximum; FWHM). This convolution concentrates the flux of unresolved structure into the central pixels of that structure, while large scale structure effectively convolves to a value near zero. Ideally, the convolved image makes stellar sources easy to identify with a simple threshold search. Unfortunately, numerous false sources are found by this algorithm among filamentary and other nonuniform structure in the bright nebulosity associated with the Galactic plane, and regions of star formation more generally (e.g. Megeath et al. 2004). In PhotVis (v1.10), the standard DAOFIND algorithm has been enhanced to include empirical estimation of a noise map for the Gaussian-convolved source detection image. Specifically, the absolute value of the convolved image is boxcar median-smoothed with a box size of five times the FWHM of the point spread function (PSF). The original Gaussian-convolved image is then divided by this noise map, effectively converting the search threshold from a signal-based threshold into an approximate local signal-to-noise-based threshold. We use a threshold value of seven in the local noise map scale, based on considerable testing on MIPS 24μm data of star-forming regions (e.g. Gutermuth et al. 2008, 2009; Beerer et al. 2010; Megeath et al. 2012). The resulting algorithm simultaneously achieves excellent sensitivity in dark, uniform, uncrowded regions of images and automatic adaptation to less sensitive local conditions, largely mitigating the production of false sources associated with nebu-

lous structure (Gutermuth et al. 2008).

Once sources are found, their flux is measured using synthetic aperture photometry via *aper.pro* from the IDL Astronomy Users' Library (Landsman 1993). The MIPSGAL tiles are made of merged observations at a range of spacecraft rotation angles, thus we chose to use aperture photometry rather than PSF-fitting photometry due to its computational simplicity and measurement robustness under that circumstance. We adopt aperture and inner and outer sky annulus radii of $6.35''$, $7.62''$, and $17.78''$ respectively, and a magnitude zero point of 14.525 mag (Vega standard) for a 1 Digital Number per second (DN/s) source observed at $24\mu m$ (Gutermuth et al. 2008)[2]. The photometric uncertainty is derived from calculations of the shot noise in the aperture and shot noise and internal variance in the sky annulus pixels that are used to compute the background emission per pixel for subtraction from the aperture flux. An internal noise floor of 0.02 mag is enforced to prevent rare data anomalies from yielding untenable uncertainty estimates.

Finally, as a characterization of source quality, we compute the FWHM of each source. As noted above, calibration of aperture photometry includes a correction for the finite sampling of the PSF set by the choice of aperture and sky radii. If an object is intrinsically resolved beyond the instrument resolution, then the source would be of relatively poor photometric quality in our catalog because the aperture correction would be incorrect. The measurement algorithm used is entirely empirical, extracting the half of peak flux radial distance from a cubic spline interpolation of the radial profile (Barth 2001). We azimuthally average (by median) the radial profile before running this algorithm to improve measurement success probabilities near structured nebulosity.

---

[2]The original Gutermuth et al. (2008) magnitude zero point is 14.6 mag. We have applied a 0.075 mag reduction to account for the sightly smaller aperture radius here relative to that work. Under the assumption of a 'FLUXCONV' value of 0.0447 MJy/sr per DN/s and a Vega flux of 7.17 Jy at the MIPS $24\mu m$ channel's isophotal wavelength of $23.68\mu m$, our zero point results in an aperture correction factor of 1.63. The MIPS Instrument handbook suggests an aperture correction of 1.61 for a $7''$ aperture, thus our slightly larger correction for our slightly smaller aperture radius ($6.35''$) is consistent.

2.2. Archive Construction

Once the source lists and photometry have been obtained from all of the individual tiles, we combine them into a unified survey "archive" data product. The tiles were constructed with some degree of overlap, thus duplicate detections near tile edges are common and must be identified and removed. Once astrometry systematics were treated (see Section 2.3), a simple angular offset tolerance of $1''$ is used to identify all inter-tile duplicates. For each set, the instance of the source that is furthest from tile edges is selected to represent that source in the final combined source list as this maximizes the coverage of the sky annulus and the surrounding area for the noise map calculation. The resulting tally of detections in the final archive that have <0.33 mag uncertainty at $24\mu m$ is 1,353,228. This requirement is approximately a Signal-to-Noise Ratio (SNR) of 3, significantly lower than the approximate SNR> 7 limit mentioned above for our empirically derived noise map in the source identification process. The photometrically determined uncertainty is generally somewhat higher because it includes photon shot noise. Ultimately, the photometric SNR limit is a sensitivity limit, but not where the survey is *complete*, as we will explore in Section 4, below. In Figure 1, the variations of magnitude uncertainties (top) and FWHM (bottom) with magnitude for the archive sources are expressed as two-dimensional histograms. The spread in magnitude uncertainty for a given value of [24] simply reflects the variation of backgrounds throughout the MIPSGAL field.

Via automated queries to the Vizier online catalog service, we obtain all of the 2MASS, GLIMPSE, and WISE sources that fall within each tile. These are matched to our MIPSGAL archive such that the closest match within an angular tolerance of $2''$ is linked to each $24\mu m$ source. The matching tallies for each data source are summarized in Table 1. A counterpart is found in at least one of these catalogs for over 94% of sources in the archive. To gauge mismatch rates for each catalog, we performed simple Monte Carlo tests across the entire archive product. Taking the number of objects within 6.35" diameter reported for characterization of potential beam contamination for each archive source (reported in the source table), we compute the mean density of sources near

each object. Note that this includes the matched source. Thus if this is a true match, we will be overestimating the field density somewhat (10-50% for GLIMPSE and 2MASS, 100% for WISE, typically). We then multiply that density by the area corresponding to the smaller 2" matching radius to determine a mean number of contaminators to expect for that source. Using the mean contaminator rate, we pull random Poisson deviate numbers of potential contaminators for each object. For each object with a non-zero synthetic contaminator count n_i in a given realization, we draw that number of uniform, area-weighted deviates (i.e. radius PDF = 2r, per the classic dartboard problem) and compare the smallest value to the radial separation, r_{match}, of the actual match for the archive source. If the nearest false source is within $r_{match} + 0.1''$ we count that as a possible contamination event in the test. We then integrate contamination counts over the entire archive, over 1000 trials. The resulting estimated mismatch rate is ~0.1% for each catalog (see Table 1).

Source quality flags are compiled for each source, including the FWHM (described above), a binary flag to note sky annulus overlap with image edges, coverage edges, or saturated pixels, and source proximity among nearest neighbor archive members, in arcseconds. An internal confusion flag based on the nearest neighbor distance and the difference in 24μm magnitude between source and neighbor is described in Section 2.3. We also tabulate the number of objects in each external catalog that fall within 6.35" of the source's centroid position.

2.3. Astrometric Systematics

Initial efforts to incorporate publicly available external catalogs with our 24μm archive revealed systematic offsets in the astrometric calibration of the MIPSGAL tiles. These offsets are shown in Figure 2 as astrometric residuals between the GLIMPSE and 24μm centroid positions ($\Delta RA(i) = [RA_{MG}(i) - RA_{GL}(i)] \, cos(Dec_{GL}(i))$; $\Delta Dec(i) = Dec_{MG}(i) - Dec_{GL}(i)$) for all unconfused matches (specifically, we require one unique GLIMPSE source within 2", and no other GLIMPSE sources within 6.35") in the archive as a function of Galactic Longitude. Many of these offsets are greater than 0.5" and much larger than the expected random error between centroid dif-

ferences. The bulk of the deviations can be cured with a constant RA-Dec offset corresponding to the median of the offsets in each tile. These tile-specific offsets have been applied to each tile's source catalog. Figure 2 shows the residuals after the application of the offset. The applied offsets and the final RMS residuals in RA and Dec for each tile are recorded in Table 2. A similar issue was reported in the Galactic center MIPS coverage in Hinz et al. (2009), and was addressed in a similar manner, using 2MASS for reference astrometry instead of GLIMPSE. Additional astrometric systematics internal to many tiles are present, but treating these would most likely require rebuilding the tiles from the BCD data products.

We identified a secondary issue related to astrometry in the archive's nearest neighbor distance (d_{NN}) distribution shown in Figure 3. The functional form of the distribution is approximately log-normal, with a narrow true normal excess centered on 10" angular separation. That distance corresponds to the central radius of the first diffraction ring outside of the Gaussian core of the MIPS 24μm PSF, suggesting that one of the pair could be a false identification. Moreover, such a feature can skew the photometry and astrometry of faint sources that fall near the feature. The magnitude difference between each source and its nearest neighbor in the archive versus d_{NN} is displayed in Figure 4a. The same data are plotted for those objects without and with GLIMPSE counterparts within 2" in Figs. 4b and 4c, respectively. The distribution of magnitude differences for sources without GLIMPSE counterparts exhibits clear excess source counts in three distinct locations: -0.2< $\Delta[24]$<0.2 & d_{NN} <8", $\Delta[24]$>0.8 & 9"< d_{NN} <11", and $\Delta[24]$>2.8 & 25"< d_{NN} <27.5". This excess is further illustrated in Figure 4d that shows the ratio of the magnitude differences of sources without and with GLIMPSE counterparts and normalized by the expected ratio uncertainty, assuming Poisson counting statistics. Guided by this figure, where the grayscale has been set to mark >3σ regions as black, we define the conditions for the internal confusion flag. The conditions and the source counts affected are listed in Table 3.

2.4. Catalog Construction

The archive data product is meant to be an inclusive list of $24\mu m$ point-like sources extracted from the MIPSGAL survey. A higher reliability subset of the archive sources, the "catalog" data product, is selected to mitigate the systematic issues in the archive discussed in Sections 2.2 & 2.3. First, we impose a more stringent <0.20 mag uncertainty requirement (SNR∼5). Then, we require a confined range of source FWHM, with thresholds that are flared to a wider range for dimmer sources to allow for their larger FWHM variance. These two stricter limits are drawn in Fig. 1, and they yield the vast majority of the archive objects that get culled from the catalog, roughly evenly divided between the two constraints. In addition, we require that the binary confusion and edge flags must be zero to ensure that these relatively rare instances are also culled from the catalog. All of the requirements for catalog inclusion are listed in Table 4. There are 933,818 sources that meet these more restrictive requirements. A counterpart in at least one of WISE, 2MASS, or GLIMPSE is found for over 98% of sources in the catalog, compared to 94% in the archive.

3. Archive and Catalog Verification

The MIPSGAL survey lacks any deep observations of verification fields to enable direct evaluation of the effectiveness and reliability of our source detection, astrometry and photometry algorithms, as is often done by large, shallow surveys such as 2MASS (Skrutskie et al. 2006). Here we perform several analyses of our methods by comparison to other previous studies and surveys in order to bootstrap some measures of reliability for extracted sources.

In Figure 5, we present the magnitude versus uncertainty distribution and magnitude histogram for the entire survey, as well as for two regions of the survey that are chosen to demonstrate the extremes in sensitivity changes set by location within the Galactic plane: the densely populated regions of the inner bulge and central disk, and the less densely populated off-plane areas of the wider survey. We have defined Galactic coordinate cuts of $|b| < 0.5$ and $|l| < 10$ for the "Central Bulge" region, and $|b| > 0.5$ and $|l| > 15$ as the "Disk, Off-Plane" zone. We use these divisions in several

figures through the rest of this paper. In summary, the one magnitude relative shift (7 vs 8) in the locations of the peaks of the magnitude histograms is an initial demonstration of the substantially reduced sensitivity of the bulge area of the survey relative to the off-plane zone. With reduced crowding, less bright sources, and less nebulosity, the off-plane portion of the survey is much more sensitive to fainter objects.

3.1. Robitaille et al. 2008

In order to verify the photometric performance and calibration of our source extraction process, we merged the MIPS $24\mu m$ photometry of red sources provided in Robitaille et al. (2008) (R08) with our catalog. The base image dataset is the same in both cases, but R08 used the original Spitzer Science Center pipeline-reduced mosaics for their photometry instead of the enhanced MIPSGAL-reduced tiles. Regarding source extraction, they also used PSF fitting photometry by hand, instead of automated aperture photometry as we have done here. Of the 18,949 red GLIMPSE sources in the R08 catalog, 16,469 have reported MIPS $24\mu m$ fluxes and uncertainties. Matches for 16,079 of those sources are made within the archive product (97.6%), and 14,926 matches (92.8%) with the catalog product. The magnitude residuals between the R08 photometry and ours are plotted in Figure 6. The 2D histogram grayscale shows the magnitude residuals to R08 matches in the archive, and the contours represent a similar 2D histogram that uses the catalog product instead. The mean zero-point calibration offsets are -0.07 mag and -0.09 mag, and the RMS deviations are 0.19 mag and 0.14 mag for the archive and catalog products, respectively. In summary, we find that our photometry agrees well with the limited photometric sample of R08.

3.2. Hinz et al. 2009

As a secondary check, we merged our archive with the MIPS $24\mu m$ photometry of the Galactic center region from Hinz et al. (2009) (H09). As with R08, the image datasets are the same as ours, but the image data treatment and source extraction differ. In this case, the image data were processed with the MIPS instrument team's DAT software (Gordon et al. 2005), and the photometry was extracted via PSF fitting. The benefit of

this reference catalog over that of R08 is that it is a complete catalog of 24μm sources from the region in question, instead of targeted photometry of red 2MASS and GLIMPSE sources across the entire inner Milky Way. As such, it is a good test of our completeness within one of the most challenging parts of the survey. Of the 120,883 sources in Hinz et al. (2009), we have 82,832 and 68,608 coincident sources in our archive and catalog products, respectively. Obviously, this is a substantial miss rate. In Figure 7, we plot the magnitude residuals versus magnitude in the top plot, demonstrating largely consistent photometry among matches. Thus while the photometry appears to agree, the issue of the discrepant sources demands further characterization.

In order to fairly examine the sources within a well-covered region, we first crop both the H09 catalog and our archive to an easily defined common coverage region of $-3 < l < 4$ and $|b| < 0.5$. Within this region, we find 63,129 and 51,937 sources from the H09 catalog and our archive product, respectively. Among those two source lists, 39,910 sources match. The bottom panel of Figure 7 shows the relative detection fraction per 1 mag bin among the matched sources (solid line), those found in our archive but missed by H09 (dot-dashed line), and those missed in our archive but found in H09 (dashed line) with the common coverage region. In the brightest bin, we see a clear deficit of H09 sources. Generally, those with marginally detectable peak saturation are rejected by the PSF fitting of H09 but are included in our archive. The range $1 < [24] < 6$ mag exhibits consistent behavior: 70% matched sources, 10% H09-only sources, and 20% H09-missed archive sources. At $[24] > 6$ mag, the fraction of sources rapidly becomes dominated by the H09 source counts, as our archive loses completeness (characterized in detail in Section 4, below). We visually inspected some of the faint H09 source positions in the MIPSGAL tiles and found that the vast majority of those that we viewed are not apparent in those data. This effort was sufficient to cement our confidence in our method's omission of these fainter sources. Further investigation of the veracity of the faint H09 sources is beyond the scope of this paper.

3.3. WISE 22μm

Finally, the merger of the MIPSGAL archive with the all-sky WISE catalog enables a check for general agreement between our photometry and the WISE 22μm photometry on a larger sample of objects. We find that 368,956 objects have reported <0.33 mag uncertainties in both the MIPS-GAL archive and WISE 22μm catalogs. We plot the magnitude residuals versus WISE 22μm magnitude in Figure 8. The median residual for bright sources ([24]<3 mag) in the "Disk, Off-Plane" field is -0.07 mag, similar to the offset to the MIPSGAL photometry reported in R08 and discussed above. The bias toward brighter values in the faint source WISE photometry is frequently observed in lower relative resolution data, where structured nebular emission is more likely to contaminate the photometric aperture relative to the surrounding sky in some sources, resulting in background flux underestimation and source flux overestimation (e.g. Gutermuth et al. 2009). In this case, the WISE 22μm fluxes of some sources are found to be as much as 3 mag brighter than the MIPSGAL photometry.

4. Completeness Characterization

The general means to test the effective sensitivity of a given photometric survey dataset and a given source extraction and analysis algorithm is to add false sources to the data and attempt to recover them. Many papers have acknowledged spatial variations in such completeness tests, but few have presented a detailed characterization. One recent effort to characterize and treat this effect was performed as part of the analysis of the *Spitzer* survey of the Orion Molecular Clouds (Megeath et al. 2012). That work emphasized probing locations near where objects of interest, YSOs in this case, have already been detected. As with any nearby star-forming region, the 24μm Galactic plane has many areas of bright and structured nebulosity where point source sensitivity will be reduced. Any catalog produced from these data would only be complete with respect to this spatially varying point source sensitivity, and thus the impact of this effect is important to characterize in some detail (e.g. Gutermuth et al. 2005; Megeath et al. 2012).

Many science goals, such as constructing lu-

minosity functions or analyzing source clustering, demand a spatially unbiased characterization of varying completeness. We have mapped this effect and provide it as a companion to the point source catalog and archive products. To quantify source completeness, we have adopted and updated the method described in Gutermuth et al. (2005) for this purpose, at a grid sampling resolution of $1' \times 1'$. The local completeness decay as a function of source flux in each grid cell is evaluated by performing successive trials of adding and recovering false sources of varying flux. Fluxes are sampled in 0.5 mag steps over a typical range from $0 < [24] < 10$ mag. Each $1'$ cell is sampled completely by adding sources at each position in a $3.125''$ grid within the cell, thereby Nyquist sampling the $6.25''$ FWHM beam width of the MIPS $24\mu m$ channel. The resulting total is ~ 400 sources per flux step per cell. The tally for each flux step and cell is normalized to represent a fractional completeness. For each MIPSGAL tile, a data cube of dimensions $60 \times 60 \times 20$ represents the differential completeness fraction for each cell position within the 1 deg^2 tile as a function of the ~ 20 flux steps of 0.5 mag.

In Figure 9, we plot examples of the differential completeness as a function of source flux for two contrasting locations, one with a smooth and low surface brightness background and the other with a structured and high surface brightness background. The low background case demonstrates a clear increase in sensitivity to faint sources relative to the bright, highly structured field. In addition, the rate of decay as a function of source flux varies between these two examples. Using the difference between the 20% and the 90% differential completeness limits as an estimator of this effect, there is a slower completeness decay in the less sensitive area (1.8 vs. 1.4 mag in the plotted examples). Despite the potential differences among completeness decay curve shapes, assigning a completeness value to each source in the archive is valuable as a convenient indicator of local source sensitivity. For each source, the completeness decay curve is extracted from the spatially nearest position to the source in the completeness cube. A linear interpolation of this curve is used to determine the magnitude at which 90% of the sources are successfully recovered. This 90% differential completeness limit, named "diffcomp90" here, is listed for each archive and catalog source. Since some science objectives may require higher or lower completeness percentages than 90%, the corresponding limiting magnitude can be derived from these differential completeness data cubes.

The correlations of source fluxes in the catalog with their local diffcomp90 values are shown in Figure 10 as a two-dimensional histogram. The most obvious feature of this plot is the strong linear feature where moderate to bright sources are correlated with their diffcomp90 value such that $[24]\sim$diffcomp90-1. This correlation is expected as we have sampled the completeness at such high spatial resolution relative to the large MIPS $24\mu m$ PSF. Any region of otherwise dark background will have effectively reduced sensitivity due to the presence of a relatively bright source, and that sensitivity reduction will be correlated with the flux of that source. In addition, Fig. 10 also shows that a completeness limit is not the same as a sensitivity limit. Regions of relatively bright diffcomp90 are rarely uniform within the sampling area, thus objects considerably fainter than the completeness limit are often detected. In contrast, it is unlikely that a bright source will be found in a region of high diffcomp90 magnitude, as the very presence of a moderate to bright source reduces the local completeness, as noted above.

5. Summary

We present the results of a full point source extraction from the entire MIPSGAL $24\mu m$ enhanced mosaics of the Milky Way.

- Over 1.3×10^6 sources have been identified, photometered, and characterized for source quality via FWHM and nearest neighbor distance (d_{NN}) measurements in our archive product.

- The archive source list has been matched with several complementary catalogs from the public archives (2MASS, GLIMPSE, WISE), yielding a substantial new multiple bandpass photometric resource for the community. Over 94% of the MIPSGAL sources have a counterpart in at least one of the external catalogs.

- We have used comparisons to these large surveys as well as some MIPSGAL photometry in the literature to evaluate the astrometric and photometric veracity of our archive and examine its completeness. Based on this work, constant astrometric offsets were applied to each tile.

- Ideal ranges of source quality measurements were identified from which a high reliability catalog product was constructed. The catalog is composed of over 9×10^5 sources that obey the more stringent constraints.

- We measured source detection completeness decay as a function of source flux at 1 square arcminute scale for the entire MIPSGAL 24μm survey. The data cubes (one for each MIPSGAL tile) resulting from this effort are provided as a companion product to aid in subsequent analysis of the catalog.

- The catalog and non-catalog archive source lists, as well as the completeness decay cubes in FITS format, are hosted and publicly available in the Infrared Science Archive (IRSA) at Caltech's Infrared Processing and Analysis Center (IPAC).

A. MIPSGAL 24μm Point Source Table Column Reference

Here we provide a reference listing of the columns delivered in the archive and catalog data product tables as they appear in the tables hosted in the IRSA at IPAC.

- l, b, RA, Dec: Galactic Longitude, Latitude, Right Ascension and Declination, in degrees, J2000, ICRS reference.

- Fnu_XX: Flux Density at the noted bandpass, XX, in mJy.

- sigma_Fnu_XX: Flux Density Uncertainty at the noted bandpass, XX, in mJy.

- Mag_XX: Vega-standard Magnitude at the noted bandpass, XX.

- sigma_Mag_XX: Magnitude Uncertainty at the noted bandpass, XX.

- SURVEY_NAME: Source name from the noted SURVEY (e.g. MIPSGAL, TWOMASS, WISE, or GLIMPSE) point source catalog.

- SURVEY_COUNT: The number of sources from the noted SURVEY (e.g. TWOMASS, WISE, or GLIMPSE) found within the 6.35″ MIPSGAL photometric aperture.

- d_NN: The angular separation in arcseconds between the source and its nearest neighbor within the MIPSGAL archive product.

- FWHM: Empirically measured full width at half maximum of the MIPSGAL source, in arcseconds.

- Sky_24: The background flux density measured in the sky annulus in MJy/sr.

- Comp_Lim_Fnu_24: The 90% differential completeness limit, in mJy.

- Comp_Lim_Mag_24: The 90% differential completeness limit, in Vega-standard magnitudes. Refered to as *diffcomp90* in the text.

- Edge_Flag: A binary flag set to 1 when the aperture overlaps with a masked out area of the MIPSGAL tiles, such as saturated areas or coverage edges.

- Int_Confuse_Flag: An integer flag set to 0 if unconfused, or 1, 2, or 3 to denote which of the three confusion criteria in Table 3 flagged this source.

REFERENCES

Aguirre, J. E., Ginsburg, A. G., Dunham, M. K., et al. 2011, ApJS, 192, 4

Barth, A. J. 2001, Astronomical Data Analysis Software and Systems X, 238, 385

Beerer, I. M., Koenig, X. P., Hora, J. L., et al. 2010, ApJ, 720, 679

Brunt, C. et al. 2014, in prep.

Carey, S. J., Noriega-Crespo, A., Mizuno, D. R., et al. 2009, PASP, 121, 76

Churchwell, E., Babler, B. L., Meade, M. R., et al. 2009, PASP, 121, 213

Ginsburg, A., Glenn, J., Rosolowsky, E., et al. 2013, ApJS, 208, 14

Gordon, K. D., Rieke, G. H., Engelbracht, C. W., et al. 2005, PASP, 117, 503

Gutermuth, R. A., Megeath, S. T., Pipher, J. L., et al. 2005, ApJ, 632, 397

Gutermuth, R. A., Megeath, S. T., Myers, P. C., et al. 2009, ApJS, 184, 18

Gutermuth, R. A., Myers, P. C., Megeath, S. T., et al. 2008, ApJ, 674, 336

Hinz, J. L., Rieke, G. H., Yusef-Zadeh, F., et al. 2009, ApJS, 181, 227

Hoare, M. G., Purcell, C. R., Churchwell, E. B., et al. 2012, PASP, 124, 939

Jackson, J. M., Rathborne, J. M., Shah, R. Y., et al. 2006, ApJS, 163, 145

Landsman, W. B. 1993, Astronomical Data Analysis Software and Systems II, 52, 246

Megeath, S. T., Allen, L. E., Gutermuth, R. A., et al. 2004, ApJS, 154, 367

Megeath, S. T., Gutermuth, R., Muzerolle, J., et al. 2012, AJ, 144, 192

Molinari, S., Swinyard, B., Bally, J., et al. 2010, A&A, 518, L100

Planck Collaboration, Ade, P. A. R., Aghanim, N., et al. 2011, A&A, 536, A1

Povich, M. S., & Whitney, B. A. 2010, ApJ, 714, L285

Robitaille, T. P., Meade, M. R., Babler, B. L., et al. 2008, AJ, 136, 2413

Santangelo, G., Testi, L., Leurini, S., et al. 2010, A&A, 520, A50

Schuller, F., Menten, K. M., Contreras, Y., et al. 2009, A&A, 504, 415

Skrutskie, M. F., Cutri, R. M., Stiening, R., et al. 2006, AJ, 131, 1163

Stetson, P. B. 1987, PASP, 99, 191

Stil, J. M., Taylor, A. R., Dickey, J. M., et al. 2006, AJ, 132, 1158

Tackenberg, J., Beuther, H., Henning, T., et al. 2012, A&A, 540, A113

Wilcock, L. A., Ward-Thompson, D., Kirk, J. M., et al. 2012, MNRAS, 424, 716

Wright, E. L., Eisenhardt, P. R. M., Mainzer, A. K., et al. 2010, AJ, 140, 1868
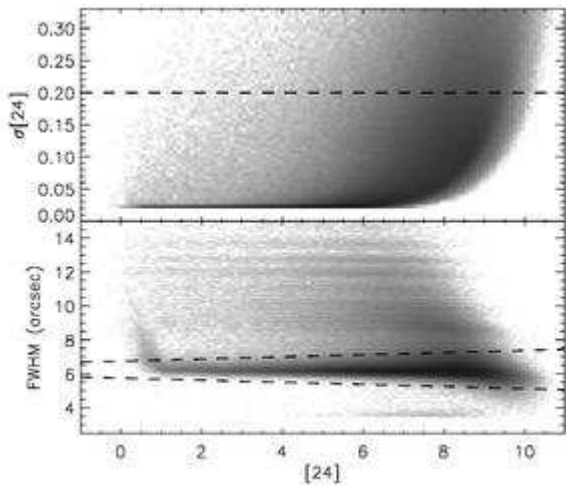
Fig. 1.— Magnitude uncertainty (top) and FWHM (bottom) versus 24μm magnitude for the entire MIPSGAL archive, plotted as a source density map. The grayscale is inverted log scale, where white is <1 and black is $>10^4$ sources per bin. Dashed lines mark the stricter limits imposed on those sources included in the "catalog" data product.
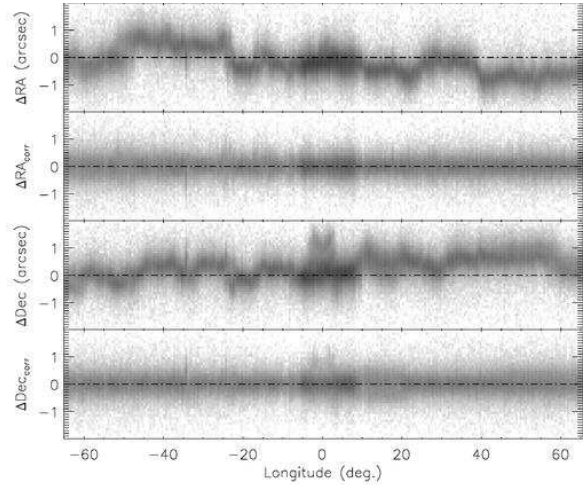
Fig. 2.— Astrometry residuals (ΔRA & ΔDec.) to GLIMPSE positions versus Galactic Longitude before and after ("corr" subscript) correction of systematic astrometric offsets by tile, plotted as a source density map. The grayscale is inverted log scale, where white is <1 and black is $>10^3$ sources per bin. Residual spread in the "corr" plots is a combination of random variance and systematic variation within tiles that is partially correlated to MIPS scan legs.
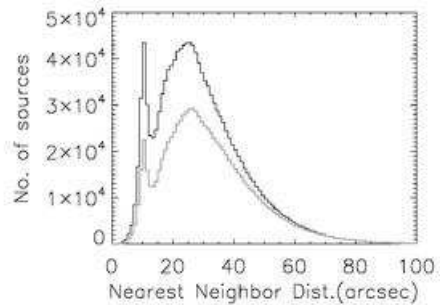
Fig. 3.— Histogram of nearest neighbor distances (d_{NN}) in arcseconds for the entire MIPSGAL archive. The black histogram is computed from all neighbor connections. For the gray histogram, we have eliminated degenerate entries caused by those object pairs that are each other's nearest neighbors.

11
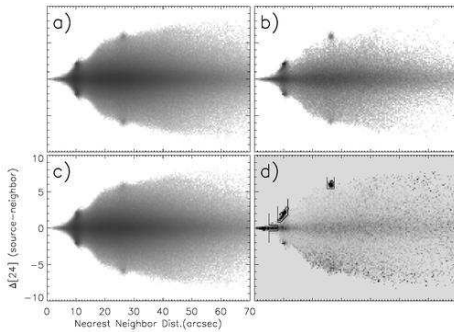
Fig. 4.— Density maps of the magnitude difference between each source and its nearest neighbor versus their separation distance in arcseconds. In panel a), we plot data for the entire archive. We split the set between those sources that lack or possess GLIMPSE counterparts in panels b) and c) respectively. Finally, panel d) shows a map of statistically significant ($>3\sigma$ in black) overdensities in panel b) relative to panel c); black lines mark our conditions for flagging a source as "confused" and therefore not included in the high quality catalog data product. The inverted grayscale is logarthmic in panels a), b), & c), with white for <1 source per bin. Black is $>10^3$ sources per bin in panel b) and $>10^4$ in a) & c). Panel d) is linear scaled from -0.5 to 3, white to black.
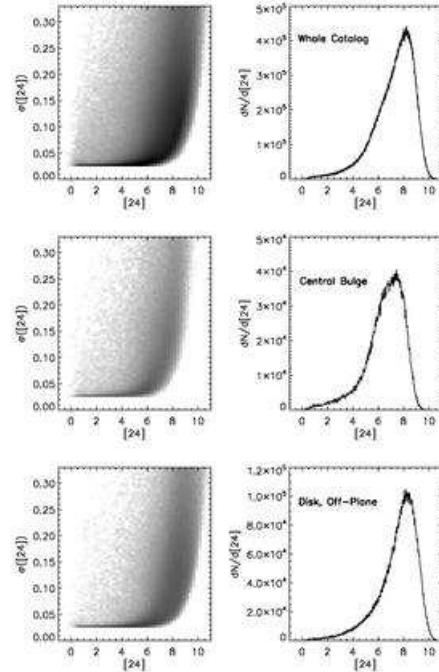
Fig. 5.— Magnitude versus uncertainty source density plots and magnitude histograms for the entire survey (top), and two of samples showing the extremes in sensitivity: the Galactic Center (middle), and the off-plane disk (bottom). The grayscale is inverted log scale, where white is <1 and black is $>10^4$ sources per bin.
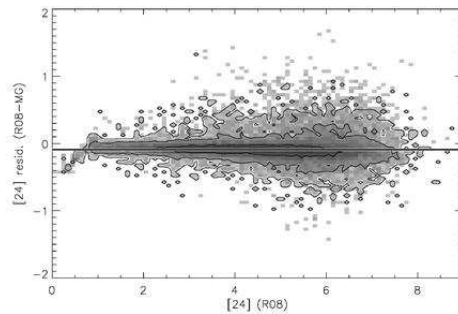
Fig. 6.— Photometry comparison of our MIPSGAL archive to the MIPSGAL photometry reported in Robitaille et al. (2008). Our calibration offset estimate is plotted as a solid line. The density map is inverted log scale, with white and black levels set to 1 and 10^3 sources per bin, respectively. Contours are plotted at 0.5, 5, and 50 sources per bin.
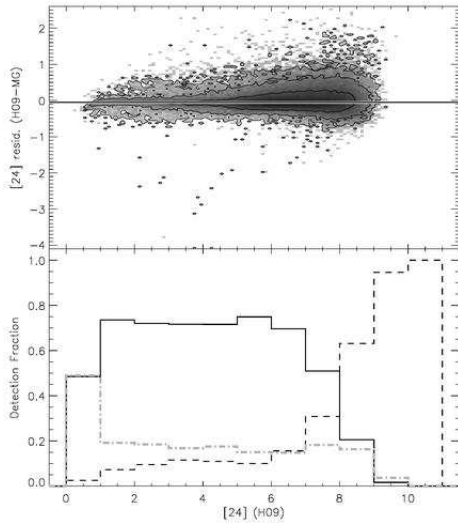
Fig. 7.— Photometry and apparent completeness comparison of our MIPSGAL archive to the MIPS-GAL photometry reported in Hinz et al. (2009). The top panel is similar to Fig. 6, above, and the source density scaling and contour levels are identical to that plot. Our calibration offset estimate is plotted as a solid line. The bottom plot contains the fraction of sources detected in our MIPS-GAL archive only (gray, dot-dashed), the H09 catalog only (black, dashed), and both data sources (black, solid), as a function of magnitude.
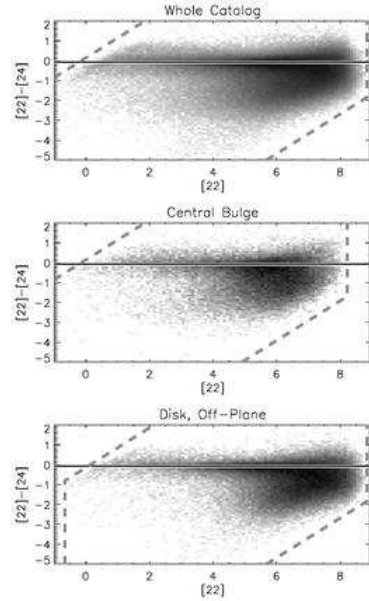
Fig. 8.— Photometry comparison to those MIPS-GAL archive sources with WISE 22μm counterparts with $\sigma < 0.33$ mag, plotted as a source density map. The grayscale is inverted log scale, with white and black levels set to <1 and $>10^3$ sources per bin, respectively. Our estimate of the offset calibration is plotted as a solid line. The approximate local saturation and sensitivity limits on the data space are marked with gray dashed lines.
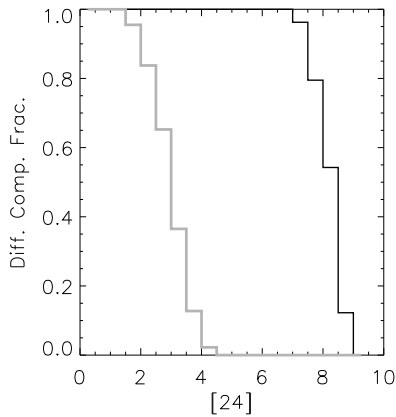
Fig. 9.— A demonstration of two differential completeness fraction decay curves found in extremes of environment. The gray plot is taken from a location of bright, structured background emission, and its 90% differential completeness limit is [24]=1.98 mag. The black plot is taken from a dim background locale, and thus it has a considerably more sensitive 90% differential completeness limit of [24]=7.44 mag.
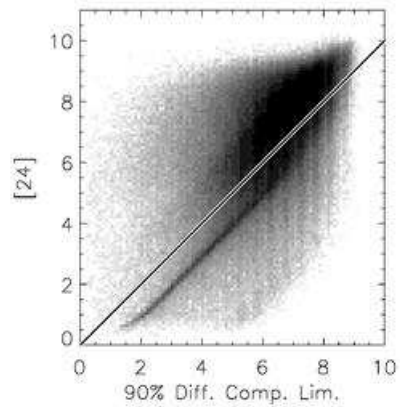
Fig. 10.— A comparison plot of catalog source fluxes to their nearest associated 90% differential completeness limit value, plotted as a source density map. The grayscale is identical to Fig. 8. Overlaid is a simple one-to-one line, for reference. The most notable feature is the diagonal linear structure at moderate to bright magnitudes, caused by the wings of the PSF these brighter sources directly creating a corresponding decay in the local sensitivity. Another feature to note is that the 90% differential completeness limit is not a single source sensitivity limit; sources can be detected to considerably dimmer values than this limit.

TABLE 1

MIPSGAL Catalog Match Summary

Data Source Name	Archive Matches	Catalog Matches	Estimated Archive Mismatches
Internal	1,353,228 (100%)	933,818 (100%)	...
2MASS	1,199,931 (88.67%)	880,168 (94.25%)	953 ± 32 (0.08%)
GLIMPSE	1,217,143 (89.94%)	867,800 (92.93%)	1240 ± 37 (0.10%)
WISE	1,138,070 (84.10%)	855,725 (91.64%)	777 ± 29 (0.07%)
Any Match	1,281,946 (94.73%)	918,966 (98.41%)	...

TABLE 2

MIPSGAL TILE ASTROMETRY OFFSETS AND RESIDUALS SUMMARY

Tile Name	ΔR.A.	ΔDec.	σR.A.	σDec.
MG0000n005	0.123	0.296	0.412	0.528
MG0000n015	-0.201	0.065	0.293	0.316
MG0000p005	0.011	0.583	0.379	0.499
MG0000p015	-0.263	0.274	0.315	0.334
MG0010n005	0.105	0.410	0.410	0.575
MG0010n015	-0.217	0.118	0.301	0.321
MG0010n025	-0.176	0.056	0.302	0.327
MG0010p005	0.122	0.625	0.362	0.513
MG0010p015	-0.167	0.233	0.299	0.324
MG0010p025	-0.229	0.089	0.316	0.343
MG0020n005	0.005	0.160	0.376	0.598
MG0020n015	-0.187	0.066	0.313	0.311
MG0020n025	-0.127	-0.039	0.313	0.326
MG0020p005	-0.009	0.679	0.338	0.521
MG0020p015	-0.054	0.183	0.301	0.316
MG0020p025	-0.207	0.242	0.311	0.325
MG0030n005	-0.121	0.018	0.377	0.459
MG0030n015	-0.204	0.063	0.306	0.311
MG0030n025	-0.142	-0.040	0.345	0.338
MG0030p005	0.034	0.402	0.335	0.601
MG0030p015	-0.046	0.096	0.317	0.325
MG0030p025	-0.143	0.149	0.316	0.340
MG0040n005	-0.287	0.060	0.367	0.382
MG0040n015	-0.212	0.021	0.307	0.318
MG0040n025	-0.140	-0.006	0.318	0.322
MG0040p005	-0.045	0.009	0.344	0.461
MG0040p015	-0.092	0.078	0.319	0.327
MG0040p025	-0.211	0.151	0.351	0.336
MG0050n005	-0.402	0.095	0.345	0.344
MG0050n015	-0.227	0.007	0.303	0.314
MG0050n025	-0.125	0.028	0.333	0.327
MG0050p005	-0.237	0.102	0.361	0.378
MG0050p015	-0.071	0.065	0.309	0.317
MG0050p025	-0.147	0.153	0.331	0.329
MG0060n005	-0.390	0.161	0.390	0.383
MG0060n015	-0.204	0.034	0.358	0.351
MG0060n025	-0.108	0.096	0.333	0.318
MG0060p005	-0.411	0.094	0.351	0.333
MG0060p015	-0.086	0.068	0.307	0.310
MG0060p025	-0.081	0.120	0.303	0.327
MG0070n005	-0.291	0.264	0.372	0.376
MG0070n015	-0.157	0.116	0.322	0.331
MG0070n025	-0.082	0.120	0.338	0.342
MG0070p005	-0.448	0.119	0.346	0.350
MG0070p015	-0.115	0.007	0.351	0.342
MG0070p025	-0.092	0.099	0.312	0.331
MG0080n005	-0.203	0.305	0.338	0.397
MG0080n015	-0.118	0.181	0.312	0.334
MG0080n025	-0.067	0.187	0.324	0.335
MG0080p005	-0.400	0.205	0.358	0.363
MG0080p015	-0.168	-0.032	0.385	0.397
MG0080p025	-0.070	0.020	0.296	0.326
MG0090n005	-0.211	0.410	0.333	0.423
MG0090n015	-0.135	0.317	0.330	0.335
MG0090p005	-0.269	0.294	0.331	0.387
MG0090p025	-0.091	-0.094	0.307	0.340
MG0100n005	-0.329	0.593	0.355	0.456
MG0100p005	-0.250	0.412	0.328	0.424
MG0110n005	-0.470	0.707	0.357	0.453

TABLE 2—*Continued*

Tile Name	ΔR.A.	ΔDec.	σR.A.	σDec.
MG0110p005	-0.388	0.564	0.346	0.448
MG0120n005	-0.537	0.556	0.375	0.458
MG0120p005	-0.426	0.635	0.329	0.434
MG0130n005	-0.532	0.450	0.381	0.444
MG0130p005	-0.448	0.571	0.343	0.433
MG0140n005	-0.493	0.366	0.377	0.445
MG0140p005	-0.457	0.458	0.359	0.433
MG0150n005	-0.420	0.358	0.377	0.451
MG0150p005	-0.460	0.383	0.323	0.414
MG0160n005	-0.427	0.377	0.353	0.429
MG0160p005	-0.444	0.385	0.325	0.403
MG0170n005	-0.449	0.330	0.374	0.437
MG0170p005	-0.356	0.337	0.381	0.441
MG0180n005	-0.409	0.396	0.373	0.424
MG0180p005	-0.389	0.338	0.348	0.423
MG0190n005	-0.602	0.485	0.385	0.428
MG0190p005	-0.454	0.445	0.351	0.432
MG0200n005	-0.632	0.553	0.372	0.401
MG0200p005	-0.556	0.569	0.355	0.419
MG0210n005	-0.698	0.572	0.375	0.364
MG0210p005	-0.633	0.573	0.349	0.410
MG0220n005	-0.561	0.459	0.394	0.381
MG0220p005	-0.768	0.574	0.372	0.373
MG0230n005	-0.507	0.439	0.388	0.383
MG0230p005	-0.646	0.506	0.391	0.377
MG0240n005	-0.514	0.508	0.394	0.379
MG0240p005	-0.405	0.400	0.383	0.397
MG0250n005	-0.306	0.474	0.387	0.396
MG0250p005	-0.217	0.291	0.381	0.385
MG0260n005	-0.188	0.309	0.390	0.382
MG0260p005	-0.214	0.345	0.371	0.381
MG0270n005	-0.117	0.271	0.397	0.381
MG0270p005	-0.213	0.340	0.411	0.393
MG0280n005	-0.079	0.170	0.380	0.369
MG0280p005	-0.112	0.284	0.413	0.401
MG0290n005	-0.054	0.223	0.368	0.405
MG0290p005	-0.035	0.169	0.412	0.384
MG0300n005	-0.117	0.384	0.374	0.403
MG0300p005	-0.090	0.162	0.363	0.388
MG0310n005	-0.130	0.512	0.405	0.422
MG0310p005	-0.152	0.328	0.407	0.415
MG0320n005	-0.084	0.597	0.358	0.388
MG0320p005	-0.179	0.418	0.348	0.395
MG0330n005	-0.063	0.637	0.358	0.402
MG0330p005	-0.117	0.457	0.353	0.393
MG0340n005	-0.131	0.692	0.378	0.397
MG0340p005	-0.117	0.528	0.361	0.381
MG0350n005	-0.231	0.664	0.364	0.400
MG0350p005	-0.094	0.573	0.350	0.389
MG0360n005	-0.211	0.607	0.355	0.374
MG0360p005	-0.150	0.586	0.358	0.374
MG0370n005	-0.245	0.556	0.376	0.396
MG0370p005	-0.225	0.587	0.354	0.380
MG0380n005	-0.323	0.523	0.381	0.394
MG0380p005	-0.302	0.587	0.363	0.371
MG0390n005	-0.503	0.552	0.367	0.418
MG0390p005	-0.586	0.718	0.396	0.394
MG0400n005	-0.829	0.637	0.418	0.389
MG0400p005	-0.728	0.744	0.342	0.390

TABLE 2—*Continued*

Tile Name	ΔR.A.	ΔDec.	σR.A.	σDec.
MG0410n005	-0.858	0.615	0.377	0.387
MG0410p005	-0.762	0.686	0.378	0.385
MG0420n005	-0.730	0.600	0.378	0.401
MG0420p005	-0.844	0.673	0.379	0.387
MG0430n005	-0.707	0.647	0.381	0.395
MG0430p005	-0.848	0.674	0.369	0.370
MG0440n005	-0.657	0.640	0.365	0.399
MG0440p005	-0.746	0.576	0.384	0.386
MG0450n005	-0.642	0.694	0.361	0.397
MG0450p005	-0.718	0.583	0.351	0.397
MG0460n005	-0.570	0.663	0.366	0.415
MG0460p005	-0.711	0.588	0.373	0.422
MG0470n005	-0.621	0.645	0.329	0.394
MG0470p005	-0.579	0.682	0.376	0.404
MG0480n005	-0.673	0.678	0.328	0.370
MG0480p005	-0.598	0.678	0.367	0.398
MG0490n005	-0.731	0.653	0.432	0.460
MG0490p005	-0.660	0.622	0.378	0.420
MG0500n005	-0.667	0.650	0.415	0.412
MG0500p005	-0.768	0.670	0.372	0.403
MG0510n005	-0.740	0.640	0.372	0.399
MG0510p005	-0.728	0.707	0.374	0.427
MG0520n005	-0.744	0.694	0.354	0.408
MG0520p005	-0.737	0.672	0.393	0.424
MG0530n005	-0.637	0.713	0.351	0.406
MG0530p005	-0.813	0.649	0.383	0.413
MG0540n005	-0.728	0.803	0.386	0.399
MG0540p005	-0.857	0.709	0.415	0.424
MG0550n005	-0.635	0.751	0.352	0.408
MG0550p005	-0.775	0.698	0.372	0.422
MG0560n005	-0.579	0.639	0.364	0.406
MG0560p005	-0.644	0.676	0.363	0.404
MG0570n005	-0.592	0.496	0.353	0.425
MG0570p005	-0.607	0.746	0.333	0.389
MG0580n005	-0.660	0.367	0.328	0.400
MG0580p005	-0.618	0.733	0.378	0.389
MG0590n005	-0.675	0.278	0.371	0.408
MG0590p005	-0.600	0.565	0.349	0.434
MG0600n005	-0.604	0.237	0.380	0.414
MG0600p005	-0.635	0.360	0.390	0.419
MG0610n005	-0.579	0.183	0.374	0.380
MG0610p005	-0.639	0.342	0.348	0.390
MG0620n005	-0.611	0.203	0.320	0.381
MG0620p005	-0.621	0.287	0.352	0.395
MG0630n005	-0.540	0.188	0.369	0.397
MG0630p005	-0.580	0.269	0.369	0.406
MG0640n005	-0.485	0.236	0.340	0.395
MG0640p005	-0.570	0.172	0.347	0.394
MG0650n005	-0.457	0.262	0.351	0.367
MG0650p005	-0.519	0.185	0.363	0.403
MG0660n005	-0.411	0.244	0.360	0.467
MG0660p005	-0.511	0.195	0.376	0.359
MG2950n005	-0.156	-0.362	0.445	0.430
MG2950p005	-0.199	-0.464	0.405	0.402
MG2960n005	-0.208	-0.246	0.421	0.432
MG2960p005	-0.085	-0.432	0.380	0.334
MG2970n005	-0.250	-0.019	0.414	0.403
MG2970p005	0.004	-0.424	0.388	0.329
MG2980n005	-0.263	-0.007	0.437	0.409

TABLE 2—*Continued*

Tile Name	ΔR.A.	ΔDec.	σR.A.	σDec.
MG2980p005	-0.011	-0.420	0.379	0.377
MG2990n005	-0.312	-0.059	0.431	0.405
MG2990p005	-0.172	-0.251	0.444	0.445
MG3000n005	-0.356	0.041	0.407	0.379
MG3000p005	-0.308	-0.093	0.409	0.395
MG3010n005	-0.340	0.099	0.407	0.339
MG3010p005	-0.320	0.036	0.418	0.358
MG3020n005	-0.276	0.103	0.410	0.369
MG3020p005	-0.311	0.110	0.399	0.372
MG3030n005	-0.226	0.023	0.430	0.394
MG3030p005	-0.345	0.038	0.394	0.369
MG3040n005	-0.122	-0.057	0.411	0.385
MG3040p005	-0.250	0.010	0.402	0.360
MG3050n005	-0.068	-0.056	0.432	0.401
MG3050p005	-0.173	-0.027	0.426	0.397
MG3060n005	-0.127	-0.038	0.404	0.354
MG3060p005	0.013	-0.155	0.420	0.385
MG3070n005	-0.128	-0.063	0.379	0.380
MG3070p005	0.056	-0.263	0.386	0.351
MG3080n005	0.022	-0.173	0.443	0.396
MG3080p005	-0.000	-0.295	0.393	0.368
MG3090n005	0.272	-0.168	0.481	0.409
MG3090p005	-0.114	-0.290	0.414	0.372
MG3100n005	0.493	-0.035	0.455	0.386
MG3100p005	-0.081	-0.288	0.413	0.363
MG3110n005	0.638	0.059	0.430	0.409
MG3110p005	0.099	-0.209	0.482	0.432
MG3120n005	0.659	0.038	0.439	0.400
MG3120p005	0.348	-0.161	0.499	0.402
MG3130n005	0.664	0.021	0.403	0.363
MG3130p005	0.604	-0.012	0.432	0.393
MG3140n005	0.687	0.077	0.394	0.360
MG3140p005	0.750	0.102	0.399	0.378
MG3150n005	0.665	0.202	0.379	0.377
MG3150p005	0.697	0.231	0.390	0.360
MG3160n005	0.633	0.368	0.373	0.390
MG3160p005	0.597	0.255	0.370	0.350
MG3170n005	0.577	0.405	0.414	0.411
MG3170p005	0.578	0.207	0.434	0.380
MG3180n005	0.586	0.302	0.436	0.430
MG3180p005	0.525	0.314	0.362	0.360
MG3190n005	0.646	0.276	0.404	0.397
MG3190p005	0.446	0.332	0.364	0.364
MG3200n005	0.658	0.268	0.449	0.386
MG3200p005	0.591	0.351	0.410	0.384
MG3210n005	0.515	0.354	0.404	0.390
MG3210p005	0.755	0.380	0.396	0.356
MG3220n005	0.441	0.380	0.369	0.368
MG3220p005	0.599	0.435	0.393	0.362
MG3230n005	0.413	0.194	0.378	0.398
MG3230p005	0.418	0.350	0.370	0.361
MG3240n005	0.443	0.087	0.365	0.354
MG3240p005	0.389	0.229	0.379	0.366
MG3250n005	0.473	0.049	0.371	0.374
MG3250p005	0.436	0.168	0.400	0.409
MG3260n005	0.248	0.250	0.430	0.441
MG3260p005	0.363	0.081	0.414	0.452
MG3270n005	0.503	0.168	0.433	0.432
MG3270p005	0.424	0.003	0.397	0.395

TABLE 2—*Continued*

Tile Name	ΔR.A.	ΔDec.	σR.A.	σDec.
MG3280n005	0.481	0.283	0.404	0.410
MG3280p005	0.453	0.112	0.400	0.409
MG3290n005	0.421	0.385	0.351	0.377
MG3290p005	0.435	0.218	0.383	0.400
MG3300n005	0.347	0.408	0.348	0.377
MG3300p005	0.448	0.326	0.370	0.391
MG3310n005	0.343	0.373	0.407	0.424
MG3310p005	0.426	0.382	0.390	0.379
MG3320n005	0.381	0.339	0.416	0.402
MG3320p005	0.352	0.420	0.383	0.394
MG3330n005	0.462	0.311	0.481	0.467
MG3330p005	0.353	0.391	0.399	0.384
MG3340n005	0.577	0.306	0.396	0.389
MG3340p005	0.404	0.315	0.396	0.377
MG3350n005	0.391	0.130	0.515	0.415
MG3350p005	0.520	0.360	0.369	0.356
MG3360n005	-0.114	-0.116	0.446	0.409
MG3360p005	0.419	0.418	0.434	0.420
MG3370n005	-0.195	-0.370	0.379	0.403
MG3370p005	0.171	0.139	0.477	0.450
MG3380n005	-0.330	-0.230	0.389	0.407
MG3380p005	-0.309	0.078	0.399	0.400
MG3390n005	-0.354	-0.128	0.374	0.366
MG3390p005	-0.410	-0.060	0.361	0.371
MG3400n005	-0.364	-0.142	0.398	0.399
MG3400p005	-0.384	-0.078	0.381	0.371
MG3410n005	-0.385	-0.138	0.372	0.381
MG3410p005	-0.392	-0.160	0.338	0.333
MG3420n005	-0.344	-0.128	0.346	0.355
MG3420p005	-0.391	-0.188	0.351	0.363
MG3430n005	-0.112	0.008	0.394	0.369
MG3430p005	-0.330	-0.088	0.371	0.365
MG3440n005	0.000	0.186	0.396	0.353
MG3440p005	-0.332	-0.023	0.348	0.351
MG3450n005	-0.013	0.297	0.380	0.376
MG3450p005	-0.098	0.167	0.383	0.371
MG3460n005	-0.099	0.209	0.403	0.377
MG3460p005	0.011	0.170	0.383	0.383
MG3470n005	-0.250	0.158	0.366	0.341
MG3470p005	-0.097	0.211	0.381	0.360
MG3480n005	-0.249	0.217	0.329	0.344
MG3480p005	-0.181	0.219	0.366	0.358
MG3490n005	-0.260	0.201	0.351	0.365
MG3490p005	-0.201	0.197	0.355	0.365
MG3500n005	-0.313	0.174	0.349	0.364
MG3500p005	-0.253	0.159	0.354	0.363
MG3510n005	-0.377	0.173	0.374	0.359
MG3510p005	-0.293	0.135	0.418	0.368
MG3520n005	-0.332	0.104	0.375	0.404
MG3520n025	-0.002	1.089	0.311	0.338
MG3520p005	-0.351	0.172	0.382	0.351
MG3520p015	-0.230	0.007	0.317	0.345
MG3530n005	-0.239	-0.049	0.357	0.361
MG3530n015	-0.125	-0.061	0.309	0.359
MG3530p005	-0.346	0.131	0.396	0.397
MG3530p015	-0.235	0.077	0.407	0.368
MG3540n005	-0.276	-0.070	0.349	0.343
MG3540n015	-0.119	-0.071	0.333	0.371
MG3540p005	-0.328	-0.025	0.337	0.359

Tile Name	ΔR.A.	ΔDec.	σR.A.	σDec.
MG3540p015	-0.299	0.068	0.322	0.326
MG3550n005	-0.330	-0.051	0.346	0.346
MG3550n015	-0.296	-0.020	0.307	0.308
MG3550n025	-0.263	-0.003	0.326	0.341
MG3550p005	-0.285	-0.043	0.349	0.349
MG3550p015	-0.219	-0.083	0.291	0.306
MG3550p025	-0.203	-0.097	0.299	0.318
MG3560n005	-0.180	0.120	0.370	0.435
MG3560n015	-0.270	0.022	0.314	0.320
MG3560n025	-0.259	0.005	0.323	0.336
MG3560p005	-0.316	-0.051	0.338	0.356
MG3560p015	-0.203	-0.096	0.298	0.311
MG3560p025	-0.145	-0.142	0.294	0.322
MG3570n005	-0.217	0.477	0.377	0.520
MG3570n015	-0.263	0.030	0.316	0.330
MG3570n025	-0.221	0.009	0.321	0.325
MG3570p005	-0.256	0.123	0.316	0.402
MG3570p015	-0.204	-0.103	0.305	0.319
MG3570p025	-0.128	-0.165	0.304	0.332
MG3580n005	-0.324	0.567	0.354	0.565
MG3580n015	-0.177	0.042	0.304	0.318
MG3580n025	-0.155	0.000	0.310	0.324
MG3580p005	-0.225	0.365	0.319	0.528
MG3580p015	-0.165	-0.068	0.288	0.328
MG3580p025	-0.154	-0.149	0.296	0.317
MG3590n005	-0.029	0.390	0.387	0.536
MG3590n015	-0.249	0.065	0.313	0.315
MG3590n025	-0.143	0.021	0.315	0.323
MG3590p005	-0.249	0.596	0.357	0.507
MG3590p015	-0.219	0.091	0.311	0.352
MG3590p025	-0.103	-0.133	0.289	0.321
MG3600n025	-0.163	0.066	0.298	0.320
MG3600p025	-0.089	-0.091	0.303	0.341

TABLE 3

MIPSGAL CONFUSION CONDITIONS

Region No.	Conditions	No. w/o GLIMPSE	No. w/ GLIMPSE	Ratio
1	$d_{NN}<5''$ OR ($d_{NN}<8''$ AND $|\Delta[24]| < 0.2$ mag)	2083	7197	0.290
2	$8.0''<d_{NN}<11.5''$ AND $\Delta[24]>0.8$ mag AND $\Delta[24]>(0.4(d_{NN}\text{-}11.5)+1.8)$ mag	3284	10767	0.305
3	$25''<d_{NN}<27.5''$ AND $\Delta[24]>5.4$ mag	355	600	0.591
Ref.	$13''<d_{NN}<25''$ AND $|\Delta[24]| < 5.4$ mag	35655	393842	0.091

TABLE 4

MIPSGAL Catalog Requirements Summary

$\sigma[24] < 0.2$ mag
$\lvert FWHM - 6.25'' \rvert < 0.5''(1 + 0.125 \times [24])$
Internal Confusion Flag $= 0$
Edge Flag $= 0$